water

MDPI

Article

High-Precision Extraction, Spatiotemporal Variations and Driving Factors of Small and Micro Wetlands (SMWs) in the Ulungur Lake Basin of China Using Sentinel-2 Imagery

Sabahat Abduriyim [1,2], Mamattursun Eziz [1,2,*] and Limin Guo [1]

[1] College of Geographical Science and Tourism, Xinjiang Normal University, Urumqi 830054, China; sabrina@stu.xjnu.edu.cn (S.A.); guolimin@outlook.com (L.G.)
[2] Xinjiang Laboratory of Arid Zone Lake Environment and Resources, Xinjiang Normal University, Urumqi 830054, China
* Correspondence: oasiseco@xjnu.edu.cn

Abstract

Small and micro wetlands (SMWs) constitute critical ecological units sustaining ecological security and biodiversity in arid regions. Nevertheless, their small patch size, fragmented distribution, and prominent inter-annual variability hinder accurate extraction, and the mechanisms governing their dynamics remain poorly understood. Taking the Ulungur Lake Basin (ULB) in Xinjiang as the study area, this study integrated multidimensional features acquired from 2019–2024 Sentinel-2 time-series imagery, including spectral bands, remote-sensing indices, tasseled-cap transformation components, textural features, and topographic variables. The Boruta algorithm and ant colony optimization (ACO) were adopted for feature selection. Random forest (RF), extreme gradient boosting (XGBoost), and support vector machine (SVM) models were then implemented under both year-by-year independent and multi-year integrated modeling schemes to extract SMWs across the study area. Sen's slope estimator, the Mann–Kendall trend test, and Geographical Detector (GD) were further applied to investigate the spatiotemporal dynamics and driving forces of SMWs. The results revealed that (1) the ACO+XGBoost model achieved optimal overall performance among the tested configurations, with a six-year mean overall accuracy (OA) of 0.923, Kappa coefficient of 0.903, and Macro F1-score of 0.919, together with low interannual variability; (2) the August-observed SMWs area showed substantial interannual fluctuation, with an endpoint difference from 2841.94 ha in 2019 to 3065.49 ha in 2024, but the monotonic trend was not statistically significant; these wetlands were mainly concentrated in lakeshore zones, along river channels and irrigation ditches, and within low-lying depressions; and (3) at the 10 km analytical scale, DEM was the dominant factor of SMWs spatial variation, whereas climate and land cover were more important at 1–5 km scales, indicating scale-dependent controls. These findings offer a technical reference for the accurate identification and dynamic monitoring of SMWs in arid regions.

Keywords: small and micro wetlands; spatiotemporal dynamics; driving factors; machine learning; Ulungur Lake Basin

Check for updates

Academic Editor: Wei Zhao

Received: 15 September 2026
Revised: 28 October 2026
Accepted: 29 October 2026
Published: 30 October 2026

Copyright: © 2026 by the authors. Licensee MDPI, Basel, Switzerland. This article is an open access article distributed under the terms and conditions of the Creative Commons Attribution (CC BY) license.

1. Introduction

SMWs are defined as natural or anthropogenic independent wetland units with an area of less than 8 ha and include small lakes, ponds, seasonal ponds, wet depressions, streams, springs, small rivers, and channels [1,2]. Compared with large and medium-sized wetlands,

SMWs represent a large numerical proportion of regional wetland units [3] and provide important ecological functions, including local climate regulation, water purification, hydrological regulation, biodiversity maintenance, pollutant interception, landscape-structure optimization, and biological habitat provision due to their large number [4]. As integral components of regional wetland systems, they provide fine-scale ecological functions such as local climate regulation and carbon sequestration [5]. Furthermore, SMWs contribute considerably to global diffusive emissions of CO_2 and CH_4 [4]. Nevertheless, their small size and scattered distribution have resulted in insufficient attention in wetland research and conservation. Since the adoption of the resolution "Conservation and Management of Small Wetlands" at the 13th Meeting of the Conference of the Contracting Parties to the Ramsar Convention in 2018, protection of SMWs has become increasingly important in global wetland governance [2,4]. In arid regions characterized by water scarcity and fragile ecosystems, these SMWs can alleviate water shortages and drought risk, improve soil moisture, and sustain the ecological water requirements of desert communities, thereby functioning as key nodes in arid-zone ecological security [6]. Their study is therefore important for maintaining the stability of desert ecosystems.

Field surveys and low-altitude aerial imagery can provide highly accurate wetland surveys, but their high costs, limited spatial coverage, and limited capacity for continuous observation constrain multi-year basin-scale analyses [7]. Satellite remote sensing overcomes many of these limitations through large spatial coverage, repeat observations, and long-term data availability [8]. Accurate identification of SMWs requires high-resolution remote-sensing imagery and high recognition accuracy. For this reason, they have long been often given insufficient attention in large-scale surveys and environmental assessment. Therefore, constructing a high-precision identification and dynamic monitoring framework for SMWs has important theoretical and practical implications for protecting the ecological safety of SMWs. However, field surveys are typically time-intensive, whereas UAV-based surveys entail high operational costs. Accordingly, remote sensing technology has emerged as an indispensable tool for wetland monitoring, benefiting from its distinctive strengths [7]. Satellite datasets present inherent trade-offs among spatial resolution, temporal resolution, and data quality. The medium-to-coarse spatial resolutions of Landsat and MODIS constrain their ability to detect small, fragmented wetlands, while revisit intervals and cloud contamination can reduce image availability during critical phenological periods [9]. In comparison, Sentinel-2 imagery combines 10 m spatial resolution with a relatively short revisit cycle, making it suitable for patch-level identification and dynamic monitoring of SMWs at regional scales [10]. Its multispectral bands cover the visible, red-edge, narrow near-infrared, and short-wave infrared regions, providing information on vegetation condition, surface water, moisture, and spatial heterogeneity that can improve wetland discrimination [11].

Feature selection in remote sensing wetland classification often relies on expert judgment or the inclusion of all available variables, which can introduce subjectivity, redundancy, high computational cost, and reduced model generalization [12]. Conventional linear dimensionality-reduction methods, such as principal component analysis and correlation-based filtering, may not capture nonlinear relationships among variables and can reduce the physical interpretability of the original features. Boruta, an all-relevant wrapper method based on random forest (RF), compares the importance of real variables with randomized shadow features to retain variables that contribute to classification; however, it may preserve many redundant features [13]. In contrast, ant colony optimization (ACO) searches the combinatorial feature space through pheromone feedback and probabilistic transition rules, allowing redundant variables to be removed while retaining physically meaningful feature combinations and thereby improving feature parsimony [14]. Machine learning classifiers combined with multi-source remote sensing features have been widely used for

wetland mapping, but performance can vary substantially with the temporal modeling strategy [15]. Year-by-year independent modeling accommodates annual climatic and hydrological conditions but may be sensitive to interannual changes in model parameters and feature importance. Multi-year integrated modeling includes a broader range of phenological and hydrological variability in the training data and can improve cross-year generalization, although it may be less responsive to short-lived extreme events. A consistent validation protocol and cross-year comparison are therefore needed to evaluate both algorithm performance and temporal robustness.

The variation of SMWs is jointly controlled by natural processes and human activities [16]. Traditional regression methods have limited ability to quantify multifactor interactions and their spatial heterogeneity [17]. The Geographical Detector (GD) model can quantify the explanatory power of individual factors for spatial differentiation without requiring a linear relationship and is therefore useful for examining wetland driving mechanisms [18]. However, many existing studies rely on a single grid scale and consequently overlook the scale sensitivity of the inferred driving mechanisms, potentially biasing interpretation.

The ULB, on the northern margin of the Junggar Basin in Xinjiang, contains numerous SMWs in lakeshore depressions, along river channels, and beside irrigation ditches. At the same time, its wetlands are influenced by mountain-basin hydrological gradients, irrigation diversion, and lake-storage regulation, making the basin well suited to remote-sensing identification, long-term change analysis, and investigation of driving mechanisms in arid environments. Using Sentinel-2 multi-temporal imagery from 2019 to 2024, this study constructed a multidimensional remote-sensing feature system based on the Google Earth Engine (GEE) platform. This study contains two main contributions. Methodologically, we developed an integrated workflow for SMWs mapping that combines ACO feature optimization with leave-one-year-out cross-validation to improve the reliability of SMWs extraction across arid inland basins. Analytically, we implemented multi-scale Geographical Detector analysis with explicit scale comparison and selection, embedding this driver assessment within the full SMW monitoring framework to disentangle scale-dependent controls of topography and hydrothermal factors on SMW dynamics. Sen's slope estimator and the Mann–Kendall trend test were then adopted to characterize temporal trends, and a multi-scale GD was applied to quantify driving mechanisms. The overall objective was to develop a high-precision monitoring framework for SMWs in arid regions and provide scientific support for wetland conservation and water-resource allocation.

2. Materials and Methods

2.1. Study Area

The Ulungur Lake Basin (ULB) lies at the southern foot of the Altai Mountains and the northern margin of the Junggar Basin, extending from 86°56′ to 88°18′ E and 46°35′ to 47°25′ N and covering approximately 5.09×10^3 km^2 (Figure 1). The basin has a typical temperate continental arid climate, with a mean annual temperature of 2.3 °C, mean annual precipitation of 129 mm, potential evapotranspiration of up to 1844 mm, a frost-free period of 110–130 days, and mean annual sunshine duration of 3157.5 h [19].

Elevation generally decreases from north to south and from east to west, with the lake surface lying at 400–482 m and terrain rising gradually toward the Altai Mountains. Under the combined effects of aridity, topographic gradients, and hydrological convergence, SMWs are concentrated in lakeshore zones, floodplains, and low-lying alluvial–proluvial fans, making the basin a representative small wetland region in arid Xinjiang. Barren land and natural grassland dominate the basin. Farmland is concentrated along the Ulungur River and the fronts of alluvial fans, whereas urban, industrial, mining, and transportation

land occurs mainly around the Ulungur Lake and along major roads. During the past three decades, expansion of farmland and built-up land, together with irrigation diversion and reservoir regulation, has altered surface hydrological processes and the spatiotemporal allocation of water resources to SMWs [20].

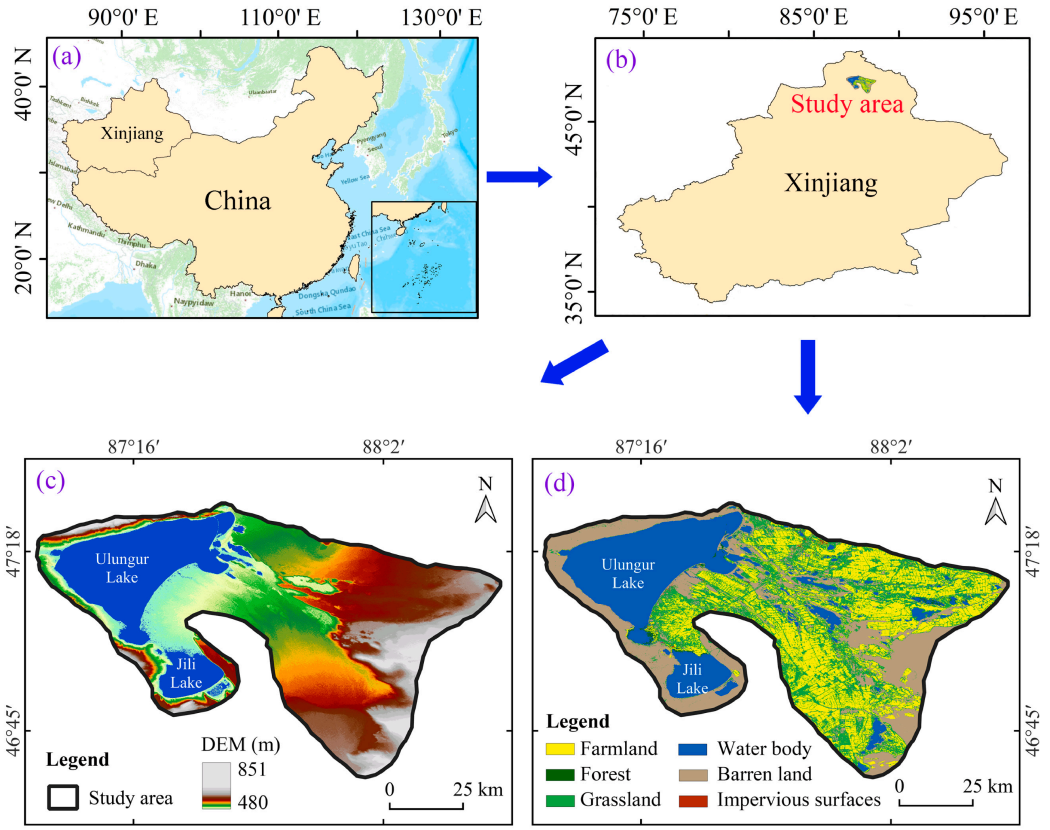


Figure 1. Map of the ULB: (**a**) map of China; (**b**) map of Xinjiang; (**c**) topography of the ULB; (**d**) land use/cover types of the ULB.

2.2. Research Data and Pre-Processing

Sentinel-2 MSI surface-reflectance imagery was chosen as the primary data source in this study. Sentinel-2 images acquired in August for each year (2019–2024) with cloud cover less than 10% were obtained via the GEE platform. August was selected because it corresponds to the peak growing season, when snowmelt recharge is complete and irrigation withdrawal is high, so wetland extent is near its annual maximum and cloud cover is relatively low; a single August composite also minimizes interannual phenological differences. All six years met the <10% cloud-cover criterion and were processed with cloud/cloud-shadow masking and median compositing. Annual August composite images were produced following cloud and cloud-shadow masking, anomalous-pixel elimination, clipping to the study-area boundary, and monthly median compositing. To retain the patch boundaries of SMWs, a consistent classification resolution of 10 m was adopted, and the 20 m red-edge and short-wave infrared bands were resampled to 10 m.

A classification feature set was then built by combining visible and near-infrared bands with remote-sensing indices, and the spatial distributions of SMWs during 2019–2024 were extracted. Climate, topographic, hydrological, land-use, and nighttime-light datasets were further integrated to generate indicators for the driving factors of SMW variations. The attributes and sources of these indicators are summarized in Table 1.

Table 1. Data types and sources.

Data Type	Product Name	Spatial Resolution	Data Source
Temperature and precipitation	CRU TS v4.06 climate dataset	1 km	National Tibetan Plateau Data Center
Evapotranspiration	MOD16A2 Version 6	500 m	NASA EOSDIS MODIS product archive
Topographic elevation	SRTM DEM v3	30 m	NASA Shuttle Radar Topography Mission/NASA LP DAAC
Land cover	China Land Cover Dataset (CLCD)	30 m	Global Land Cover Team, Wuhan University
Nighttime light	Harmonized DMSP-OLS and NPP-VIIRS nighttime light data	1 km	Harmonized DMSP-OLS & NPP-VIIRS nighttime light dataset

2.3. Feature Extraction

Based on the GEE platform and Sentinel-2 MSI imagery, the six original spectral bands (B2 (Blue), B3 (Green), B4 (Red), B8 (NiR), B11 (SWIR1), B12 (SWIR2)) were extracted. Three Tasseled-cap components, namely brightness (TCB), greenness (TCG), and wetness (TCW), were also derived to depict surface brightness, vegetation status, and surface moisture conditions. Four GLCM (gray level co-occurrence matrix) texture metrics were derived from the B8 near-infrared band: B8_contrast (contrast), B8_diss (dissimilarity), B8_ent (entropy), and B8_asm (angular second moment) [13]. The Digital Elevation Model (DEM) was incorporated as a topographic variable to depict the terrain context for wetland formation and distribution. Subsequently, five remote sensing indices were computed: Normalized Difference Vegetation Index (NDVI), Enhanced Vegetation Index (EVI), Normalized Difference Water Index (NDWI), Modified Normalized Difference Water Index (MNDWI), and Normalized Difference Moisture Index (NDMI) [13,21,22]. The red-edge bands (B5–B7) have a 20 m resolution and were not included in the candidate feature set in order to maintain a consistent 10 m classification resolution; they were not excluded after feature selection.

2.4. Feature Selection Methods

To determine the most significant features that can be used for achieving a high classification accuracy, the Boruta algorithm and ACO were adopted as two feature selection strategies. Each algorithm was executed under two modes: a year-by-year mode, which independently generates one feature subset per year and yields six subsets in total; and a pooled multi-year mode, in which all samples spanning 2019 to 2024 are aggregated to produce a single unified feature subset. Four types of feature subsets were accordingly obtained for subsequent modeling inputs: Boruta-annual, Boruta-pooled, ACO-annual, and ACO-pooled.

2.4.1. Boruta

Boruta is an all-relevant feature selection method built upon the RF algorithm. It constructs randomized shadow features from the original variables and compares the importance of each real feature against its shadow counterpart to identify variables that contribute to classification [23]. The Boruta algorithm generates shadow features by randomly permuting the input features and adding noise to them. It then compares the importance of the original input features with that of their corresponding shadow features to identify important features. The Boruta algorithm was applied independently to each subset in this

study to identify significant features. We then quantified the selection frequency of each candidate feature, defined as the proportion of iterations where the feature was deemed 'Confirmed' [13].

2.4.2. ACO

ACO is a nature-inspired algorithm. It simulates ant-foraging behavior via path selection and pheromone updating to explore the candidate feature space for feature combinations that maximize classification performance [13]. Unlike approaches relying merely on individual feature-importance rankings, ACO can take into account interactions and complementarity among features, making it suitable for identifying compact subsets from multidimensional remote-sensing variables [14]. The ACO algorithm terminates if the optimal subset is identified or a predefined number of iterations is reached, and the best feature subset is returned as output; otherwise, pheromones are updated, and a new set of ants is deployed to repeat the process [24].

2.5. Machine Learning Modeling

Using the feature subsets derived from the two feature-selection strategies, two machine-learning modeling frameworks were built employing the RF, XGBoost, and SVM algorithms.

2.5.1. RF

RF is an ensemble learning algorithm that efficiently models complex data for classification and regression. In this study, the RF model was constructed with fixed empirical parameters to ensure stable performance. The ensemble included 100 decision trees ($N_{tree} = 100$) to balance computational efficiency and error convergence. The minimum leaf size (N_{min}) was set to 5 to regularize tree depth and mitigate overfitting in high-dimensional spectral feature spaces. Node splitting adopted a random feature subset (M_{try}), following the standard regression default of one-third of the total input features [25].

2.5.2. XGBoost

XGBoost is an efficient, scalable gradient boosting framework that enhances predictive accuracy and computational efficiency. For a fair model comparison, the XGBoost ensemble size was unified with RF using 100 boosting iterations ($n_estimators = 100$). The maximum tree depth (max_depth) was set to 6 and the minimum child weight (min_child_weight) to 5 to constrain structural complexity and suppress spectral noise overfitting. A learning rate of 0.1 was employed to ensure stable convergence [26].

2.5.3. SVM

SVM is a robust supervised learning algorithm suitable for both classification and regression. It optimizes generalization performance by balancing model complexity and learning capability from limited samples. Herein, SVM classification was implemented using the radial basis function (RBF) kernel in MATLAB (v.2024). The box constraint (C) was fixed at 1, while gamma was set to $1/p$ [27].

Under the year-by-year independent-modeling scheme, training and validation samples were partitioned for each year separately, enabling the model to adapt to year-specific hydrological and vegetation-phenological conditions. For multi-year integrated modeling, samples spanning 2019–2024 were pooled to generate a unified training dataset. This approach expands the scope of phenological and hydrological variability captured within the training data and aims to enhance the cross-year generalization performance of the model.

A total of 5161 reference samples were used (2019: 863; 2020: 853; 2021: 853; 2022: 846; 2023: 860; 2024: 886), of which 3603 were used for training and 1558 for validation. The samples were generated by year-by-year visual interpretation with reference to contemporaneous high-resolution historical imagery. A class-stratified 70/30 random split was applied independently to each year (random seed 42) at the sample level; no over-sampling, under-sampling, or class weighting was used.

2.6. Accuracy Validation

Based on the confusion matrix, model performance was evaluated in terms of Overall Accuracy (OA), the Kappa coefficient, and the macro F1-score. Cross-year robustness was assessed via the six-year mean and standard deviation of these metrics [28]. The OA is defined as the proportion of correctly classified samples and reflects the general reliability of the model. It is calculated as follows:

$$\mathrm{OA} = \frac{\sum_{i=1}^{k} X_i}{N} \times 100\% \quad (1)$$

where K indicates the number of feature types, X_i represents the number of samples correctly categorized by feature type i, N denotes the total number of test samples [28].

The Kappa coefficient quantifies the consistency of classification results. Values closer to 1 correspond to high-reliability classification, whereas values below 0.4 indicate low classification reliability [29]. It is computed as follows:

$$\mathrm{Kappa} = \frac{A_0 - P}{1 - P} \times 100\% \quad (2)$$

$$P = \frac{\sum_{i=1}^{c} X_i \times \sum_{i=1}^{r} X_i}{N^2} \quad (3)$$

where r denotes the number of test samples classified by the classifier into a specific feature type, c denotes the number of test samples belonging to that feature type, and A_0 denotes the proportion of observed agreement between in-situ sampled points and threshold values extracted from images [29].

The F1-score, a key metric for evaluating the efficacy of classification models, is the harmonic mean of precision and recall. It takes into account both the proportion of correctly classified samples and the model's capacity to retrieve all positive samples [30]. It is computed as follows:

$$F = 2 \times \frac{P \times R}{P + R} \quad (4)$$

where F denotes the F1-score, with a range of 0 to 1. A value closer to 1 indicates superior model classification performance; P represents precision rate, and R represents recall [30].

2.7. Analysis of Spatiotemporal Dynamics of SMWs

A wetland classification system for the study area was formulated based on the national standard Wetland Classification (GB/T 24708-2009) [31], previous relevant wetland-classification literature [16,17], and the land-cover features of the ULB. Land-cover types were grouped into wetland and non-wetland categories. Wetlands consisted of perennial lakes, reservoirs, rivers, and marshes, while non-wetlands comprised farmland, barren land, impervious surfaces, forest, shrubland, and grassland.

The total area and patch count of SMWs within the ULB were extracted for each year, and long-term variations were compared for lakes, rivers, and marshes individually. Transition matrices among SMWs, large wetlands, and non-wetlands were then adopted to quantify spatial conversion patterns. Sen's slope estimator [32] and the Mann–Kendall trend test [33] were subsequently employed. A 1 km grid was constructed, and the Sen's

slope for SMWs area change along with its significance (p-value) was computed for each grid cell. The outputs were grouped into five classes: significant decrease, slight decrease, stable, slight increase, and significant increase.

2.8. Multi-Scale Geographical Detector Analysis

To investigate the scale dependence of factors governing the spatial differentiation of SMWs, three grid scales (1 km, 5 km, and 10 km) were defined based on the spatial extent of the study area and the native resolutions of driving variables. These scales correspond to the local micro-environment, landscape unit, and regional background, respectively. The total SMWs area within each grid cell was taken as the dependent variable.

Continuous driving variables were discretized using the optimal parameters-based geographical detector (OPGD). Four discretization algorithms, namely equal interval, quantile, geometric interval, and standard deviation classification, were tested with the number of strata constrained between 3 and 8. The optimal discretization scheme was determined based on the pooled 2019–2024 dataset at the 10 km grid scale and adopted consistently for all six years: DEM (equal interval, 8 strata), slope (quantile, 7 strata), aspect (quantile, 7 strata), ET (quantile, 6 strata), prec (equal interval, 8 strata), temp (geometric interval, 7 strata), and light (geometric interval, 8 strata). The CLCD land-cover variable was used directly with its original four categories: cropland, grassland, water body, and barren land. The number of valid grid cells ranged from 59 to 63 annually for the 10 km grid, 152 to 170 for the 5 km grid, and 1084 to 1114 for the 1 km grid.

Factor detector: The q-value was computed for each factor to quantify its independent explanatory power for the spatial variations of SMWs. Only results with $p < 0.05$ were retained for subsequent analysis. The factor detector is defined as [34]:

$$q = 1 - \frac{1}{N\sigma}\sum_{h=1}^{L} N_h \sigma_h^2 \quad (5)$$

where q denotes the explanatory power of the selected factor for the spatial variation of SMWs, ranging from 0 to 1; a larger q-value indicates stronger explanatory ability; $h = 1, 2, \ldots, L$ denotes the stratification of the selected factor; N_h and N denote the sample numbers of the entire study area and hth layer, respectively; and σ and σ_h denote the variances in the entire study area and hth layer, respectively [34].

Interaction detector: The interaction detector identifies whether the combined effects of two variables enhance or diminish the explanatory power for SMW variations. It assesses the relationships between two spatial variables by comparing their combined influence with their individual effects.

The q-statistics $q(X_1)$ and $q(X_2)$ quantify the explanatory power of individual factors X_1 and X_2, while $q(X_1 \cap X_2)$ represents the explanatory power of their pairwise interaction. Five interaction types for interaction detector are defined to describe synergistic driving relationships: nonlinear weakening $q(x_1 \cap x_2) < \mathrm{Min}(q(x_1), q(x_2))$, univariate weakening $\mathrm{Min}(q(x_1), q(x_2)) \leq q(x_1 \cap x_2) \leq \mathrm{Max}(q(x_1), q(x_2))$, bivariate enhancement $\mathrm{Max}(q(x_1), q(x_2)) < q(x_1 \cap x_2) < (q(x_1) + q(x_2))$, nonlinear enhancement $q(x_1 \cap x_2) > (q(x_1) + q(x_2))$, and independent effect $q(x_1 \cap x_2) = (q(x_1) + q(x_2))$ [35]. The optimal analytical scale was identified by comparing the explanatory power of individual factors and the number of statistically significant predictors across three grid resolutions [36]. The technical workflow of this study is illustrated in Figure 2.

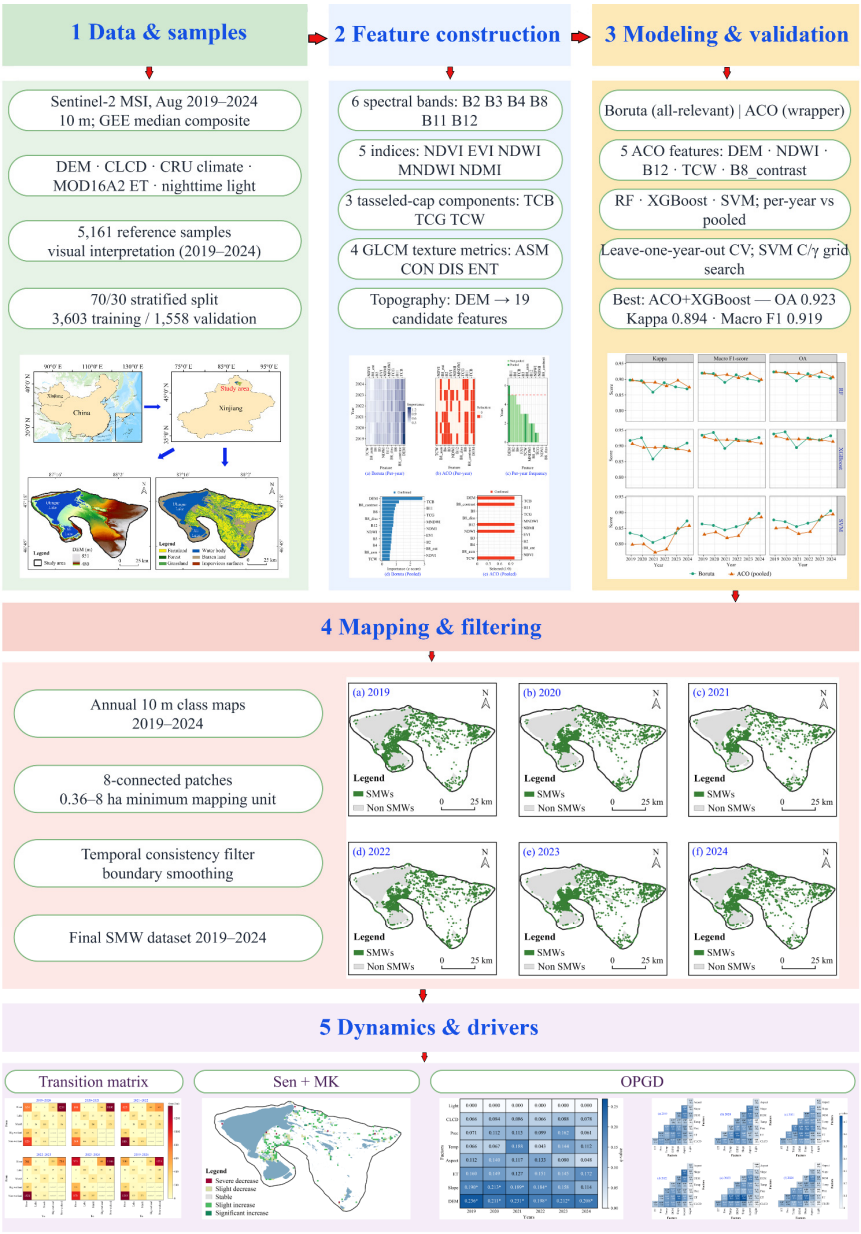


Figure 2. The technical workflow of this study.

3. Results

3.1. Feature Selection

Using Boruta and ACO, 19 candidate features (B2, B3, B4, B8, B11, B12, TCB, TCG, TCW, B8_contrast, B8_diss, B8_ent, B8_asm, DEM, NDVI, EVI, NDWI, MNDWI, and NDMI) were evaluated under both year-by-year and multi-year pooled strategies to identify a compact feature subset with strong discriminative ability for SMWs identification (Figure 3).

As shown in Figure 3, Boruta identified all 19 features as statistically significant in the pooled multi-year dataset, thereby retaining the complete set of relevant information. In contrast, ACO using classification accuracy as the optimization objective, retained only five features—DEM, NDWI, B12, TCW, and B8_contrast—corresponding to a feature compression rate of 73.7%. These five variables were also the only features selected by both algorithms in the pooled dataset, indicating that they combine statistical relevance with discriminative contribution and represent the core dimensions of topography, water and moisture conditions, and texture.

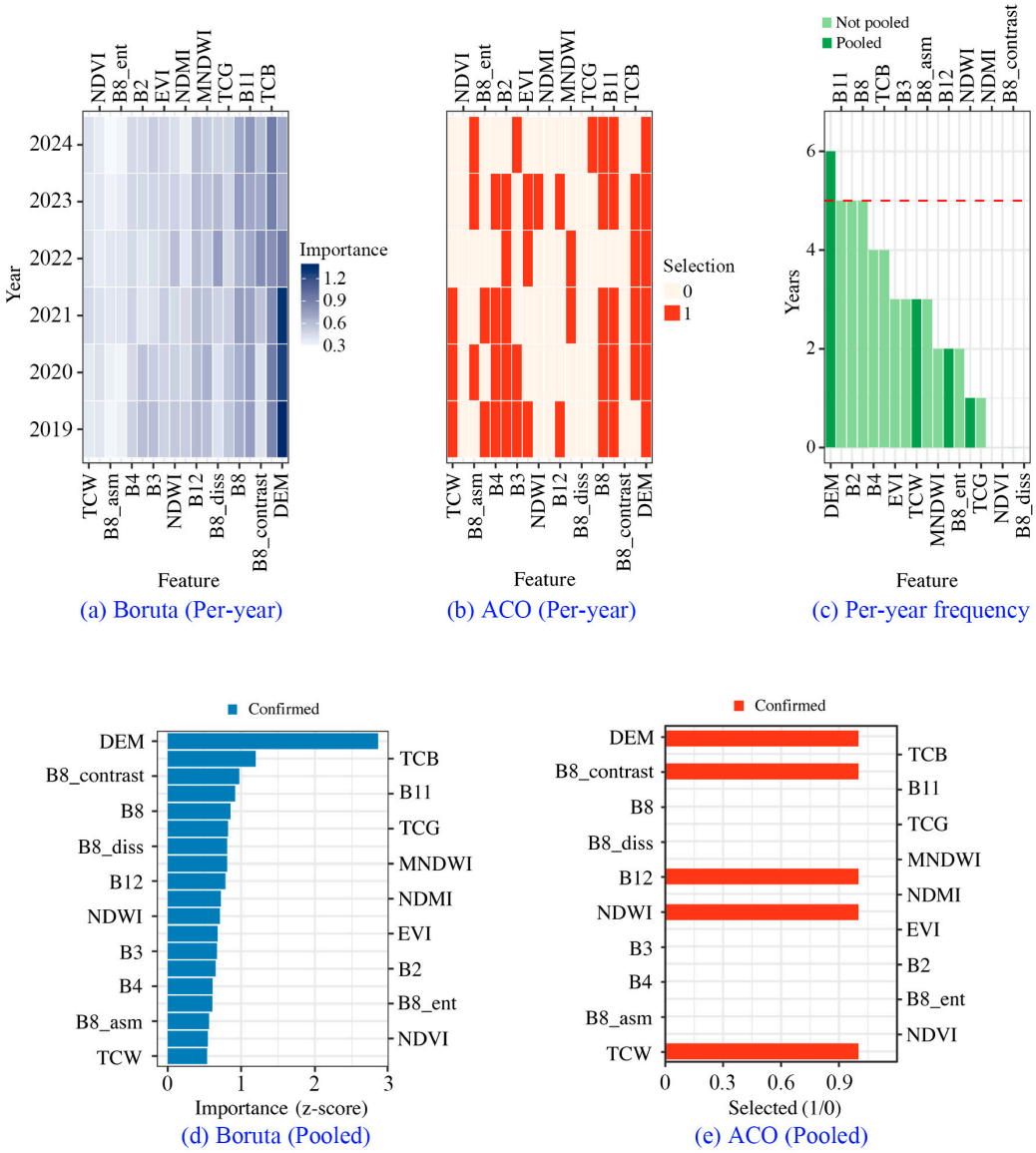


Figure 3. Feature selection results from Boruta and ACO: (**a**) year-by-year Boruta importance heatmap; (**b**) year-by-year ACO selection heatmap, where 0 and 1 denote unselected and selected features, respectively; (**c**) frequency of feature selection across years, used to evaluate temporal stability; (**d**) Boruta results for the pooled multi-year dataset, confirmed important variables are shown in blue; (**e**) ACO results for the pooled dataset, showing only the selected features in red.

At the year-by-year scale, the ACO subsets varied in size and composition, and their overlap with the pooled ACO subset was limited. Because Boruta retained all 19 features, the overlap between the two methods equals the ACO subset; Boruta therefore does not provide independent corroboration. The five ACO-selected features from the pooled strategy were more representative across years and provided a parsimonious basis for transferable classification models.

3.2. Accuracy Comparison of Multi-Strategy Machine Learning Models

Based on the feature-selection results, the extraction accuracy and stability of different feature-set and classifier combinations were evaluated under the year-by-year independent (Figure 4) and multi-year integrated (Figure 5) modeling strategies.

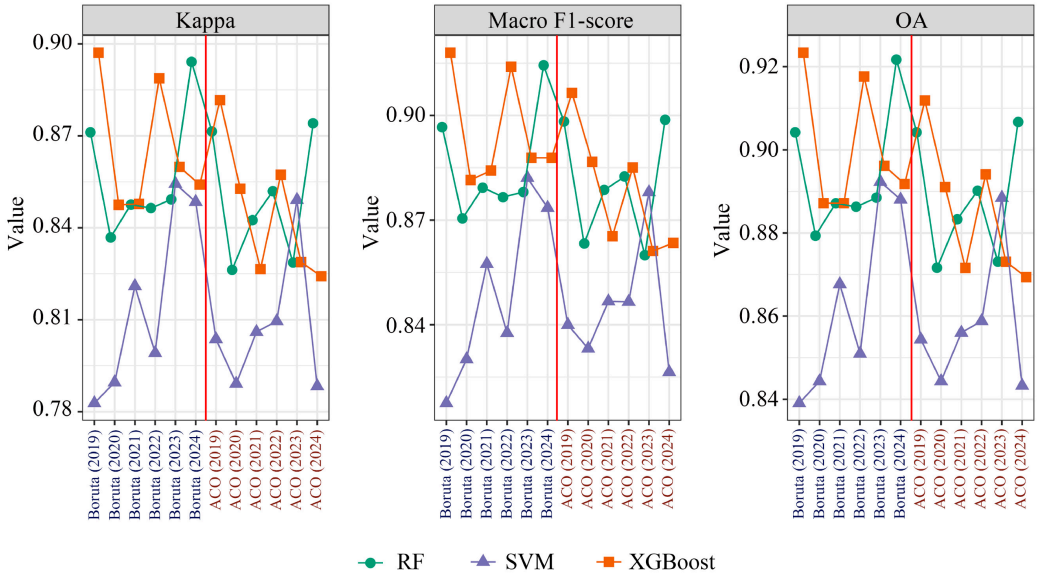


Figure 4. Comparison of year-by-year modeling accuracy.

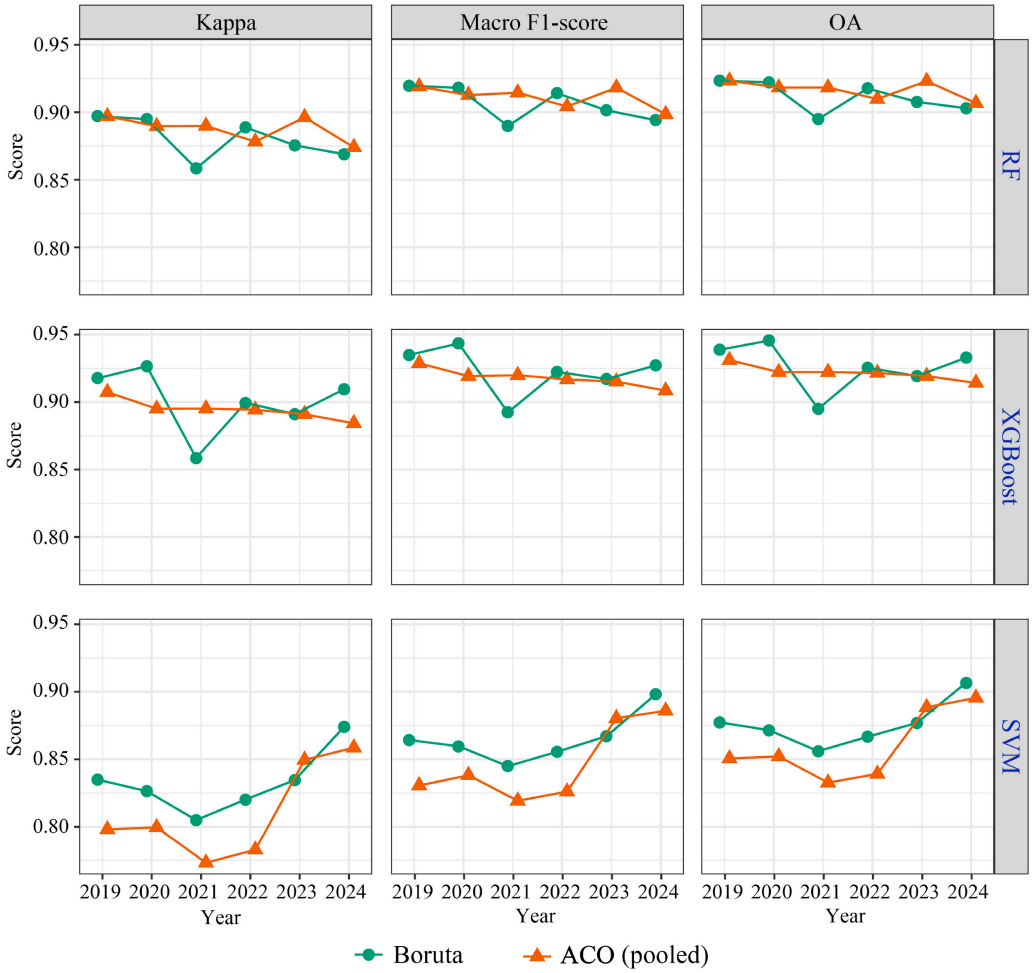


Figure 5. Comparison of multi-year integrated modeling accuracy.

As shown in Figure 4, under the year-by-year independent strategy, Boruta+XGBoost achieved a six-year mean OA of 0.893, Kappa coefficient of 0.863, and Macro F1-score of 0.889; The relevant parameters are substantially equivalent to those of Boruta+RF (OA = 0.891, Kappa = 0.866, Macro F1-score = 0.886). With the ACO feature set, mean OA, Kappa, and

Macro F1-score values were 0.884, 0.857, and 0.879 for XGBoost, respectively; while 0.887, 0.861, and 0.882 for RF, respectively. Although ACO reduced the number of features by 40–74% relative to Boruta, mean OA decreased by only 0.004 for RF and 0.009 for XGBoost. This demonstrates that feature reduction retains the majority of discriminative information while enhancing interannual consistency in model performance. SVM showed the lowest performance among all configurations, with mean OA, Kappa, and Macro F1-score values of 0.856, 0.824, and 0.843, respectively, indicating lower suitability for fine-scale extraction of SMWs in this arid-region application.

As shown in Figure 5, under the multi-year integrated strategy, all models showed improved accuracy. The XGBoost model using the Boruta feature set achieved the highest mean values (OA = 0.926, Kappa = 0.909, Macro F1-score = 0.924) across the six-year validation period. However, its OA, Kappa, and Macro F1-score values decreased in 2021 (OA = 0.895, Kappa = 0.869, Macro F1-score = 0.892) compared with the highest value recorded in 2020 (OA = 0.946, Kappa = 0.931, Macro F1-score = 0.945), indicating noticeable interannual variability. In contrast, the multi-year integrated XGBoost model using the ACO feature set achieved mean OA, Kappa, and Macro F1-score values of 0.923, 0.903, and 0.919, respectively. The results differ slightly from those of the Boruta-based model. Notably, the differences between the minimum (OA = 0.914, Kappa = 0.893, and Macro F1-score = 0.910 in 2024) and maximum (OA = 0.922, Kappa = 0.903, and Macro F1-score =0.918 in 2022) values across years are very small, demonstrating remarkable interannual stability. Overall, the multi-year ACO-based RF model achieved mean OA, Kappa, and Macro F1-score values of 0.917, 0.893, and 0.911, respectively, which were lower than XGBoost in both accuracy and stability. These results show that multi-year integrated modeling can use multi-temporal samples to improve classification accuracy. They also indicate that the five core features selected by ACO retain discriminative ability comparable to that of the full feature set while providing stronger robustness for cross-year applications.

Leave-one-year-out cross-validation, where the test year remained entirely unseen during model training, yielded a mean OA of 0.925 (Kappa = 0.899, Macro F1 = 0.921), nearly identical to the pooled modeling result. Per-class F1 scores on the held-out validation samples were 0.926 for river wetland, 0.920 for lake wetland, and 0.861 for marsh wetland; all three values were above 0.86. The paired difference between ACO+XGBoost and ACO+RF was 0.0051 (95% CI: −0.0005 to 0.0107; paired *t*-test and Wilcoxon $p = 0.063$), indicating a small and statistically non-significant difference (Supplementary Tables S5–S7).

3.3. Temporal Changes in SMWs

Using the classification results from the multi-year integrated ACO+XGBoost model, a patch-level dataset was constructed for subsequent analysis of SMW dynamics. According to the national standard Specifications for Conservation and Management of Small Wetlands (GB/T 42481–2023) [37], patches between 0.36 ha and 8 ha were defined as SMWs. The 8 ha upper limit follows the national standard, whereas the 0.36 ha lower limit corresponds to a 6 × 6 pixel window at the 10 m Sentinel-2 resolution. It also falls within the 0.3–0.5 ha range widely used for arid wetland mapping, facilitating comparison with prior work. Besides, sensitivity tests show smaller thresholds (0.09 and 0.18 ha) inflate wetland area by capturing ephemeral noisy patches; the 0.36 ha threshold balances mapping completeness and patch reliability while preserving interannual trends. This lower threshold was used to suppress isolated pixel-level noise, including residual cloud shadows and single-pixel water misclassification, while retaining most genuine SMWs patches and is consistent with a commonly used minimum mapping unit for wetland classification [7].

After annual binary wetland classifications were projected to a common coordinate system, an eight-neighborhood connected-component algorithm was used to aggregate contiguous wetland pixels into vector patches and derive their geometric attributes [38,39]. Area-based filtering was then used to remove large water bodies and isolated pixel noise [7]. To reduce artificial interannual fluctuations from year-specific classification, a time-series consistency constraint based on spatial topology between adjacent years was applied.

Same-class patches were matched across adjacent years if their spatial overlap covered ≥ 5% of the smaller patch, or if one patch's centroid lay inside the other. Temporally isolated single-year patches without an adjacent-year match and smaller than 0.5 ha were discarded, while single-year patches ≥ 0.5 ha were kept to preserve real seasonal wetlands. Boundary fluctuations were smoothed using a 3 × 3 spatial window and information from the two adjacent years: boundary pixels with no wetland support in either adjacent year and no more than 2 wetland pixels in the 3 × 3 neighborhood were removed, while non-wetland pixels with wetland support in both adjacent years and at least 7 wetland pixels in the 3 × 3 neighborhood were added and assigned the majority class. The isolated-patch step reduced annual SMW area by 2.8–7.3% and patch counts by 8.9–20.4%; boundary smoothing changed net area by less than 0.1%. The area values in Table 2 correspond to the dataset after this post-processing workflow.

Table 2. Area of different SMWs in the ULB (ha).

Year	River Wetlands	Lake Wetlands	Marsh Wetlands	Total
2019	2109.54	346.01	386.39	2841.94
2020	1857.01	329.11	399.92	2586.03
2021	1439.55	337.07	437.74	2214.37
2022	1873.81	291.74	398.55	2564.10
2023	2653.07	286.33	349.35	3288.74
2024	2268.41	357.41	439.66	3065.49

Using the multi-year integrated ACO+XGBoost model, individual lake, river, and marsh wetland units smaller than 8 ha were identified as SMWs. Annual SMWs area was then summarized for 2019–2024 (Table 2). The total area showed substantial interannual fluctuation; the endpoint difference was positive, but the monotonic trend was not statistically significant. It declined from 2841.94 ha in 2019 to a six-year minimum of 2214.37 ha in 2021, increased in the following two years to a maximum of 3288.74 ha in 2023, and then decreased to 3065.49 ha in 2024.

River wetlands accounted for the largest share of SMWs area throughout the study period, representing 74.23%, 71.81%, 65.01%, 73.08%, 80.67%, and 74.00% of the total area from 2019 to 2024, respectively. River wetland area declined from 2109.54 ha in 2019 to 1439.55 ha in 2021, recovered to 2653.07 ha in 2023, and then decreased slightly to 2268.41 ha in 2024. Its interannual variation was markedly greater than that of lake and marsh wetlands, indicating that river wetlands were the main contributor to changes in the total SMWs area. Lake wetland area varied more moderately, ranging from a minimum of 286.33 ha in 2023 to a maximum of 357.41 ha in 2024. Marsh wetland area increased from 386.39 ha in 2019 to 437.74 ha in 2021, declined to 349.35 ha in 2023, and then rose to 439.66 ha in 2024, the highest value during the six-year period.

3.4. Spatial Distribution Patterns of SMWs

Spatial distribution maps for 2019–2024 were generated in QGIS from the SMWs classification results (Figure 6). As shown here, SMWs were concentrated mainly along the shores of Ulungur Lake and Jili Lake, in low-lying depressions between the two lakes,

and along the main channel and tributaries of the Ulungur River and irrigation ditches. Persistent high-density clusters occurred along the northern, northeastern, eastern, and southeastern shores of Ulungur Lake, around Jili Lake, and in the low-lying transition zone between the two lakes. Additional scattered patches followed ditches, rivers, and seasonal watercourses in the north-central, eastern, and southeastern basin, where they formed punctate, linear, or bead-like patterns.

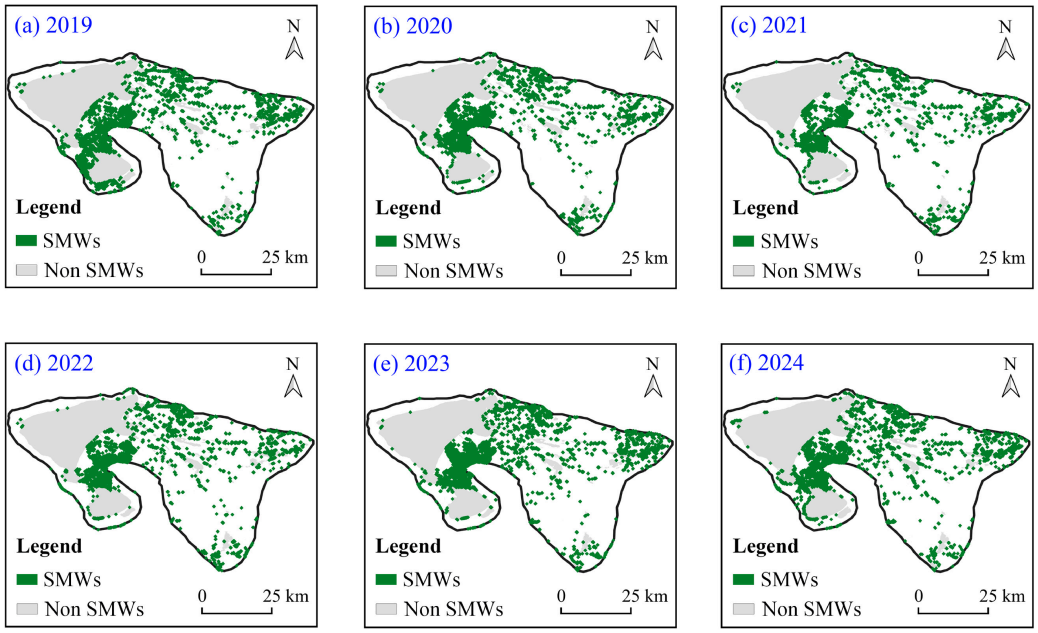


Figure 6. Distribution of SMWs in the ULB: (**a**) 2019; (**b**) 2020; (**c**) 2021; (**d**) 2022; (**e**) 2023; (**f**) 2024. Note: The trend classes are defined by |Sen's slope| > 0.5 ha/yr and |Z| > 1.96 ($p < 0.05$). The class labeled "Severe decrease" in Figure 7 corresponds to "Significant decrease" in Table 3.

Table 3. Degrees of area change for SMWs in the study area.

Class	Area (ha)	Percent (%)
Significant decrease	699.13	0.14
Slight decrease	7290.94	1.43
Stable	483,898.75	94.94
Slight increase	15,880.27	3.12
Significant increase	1897.64	0.37

Interannually, wetland patches expanded in 2020 relative to 2019, mainly along lakeshores and watercourses; they then decreased during 2021–2022 as some scattered patches contracted or disappeared. The strongest expansion occurred in 2023, particularly in lakeshore depressions, watercourse corridors, and the eastern and southeastern parts of this basin. In 2024, both wetland area and patch number declined from the 2023 peak.

Overall, the distribution and interannual change of SMWs showed strong hydrological dependence, with the most dynamic areas concentrated along lakeshores, river and ditch networks, and low-lying moist zones.

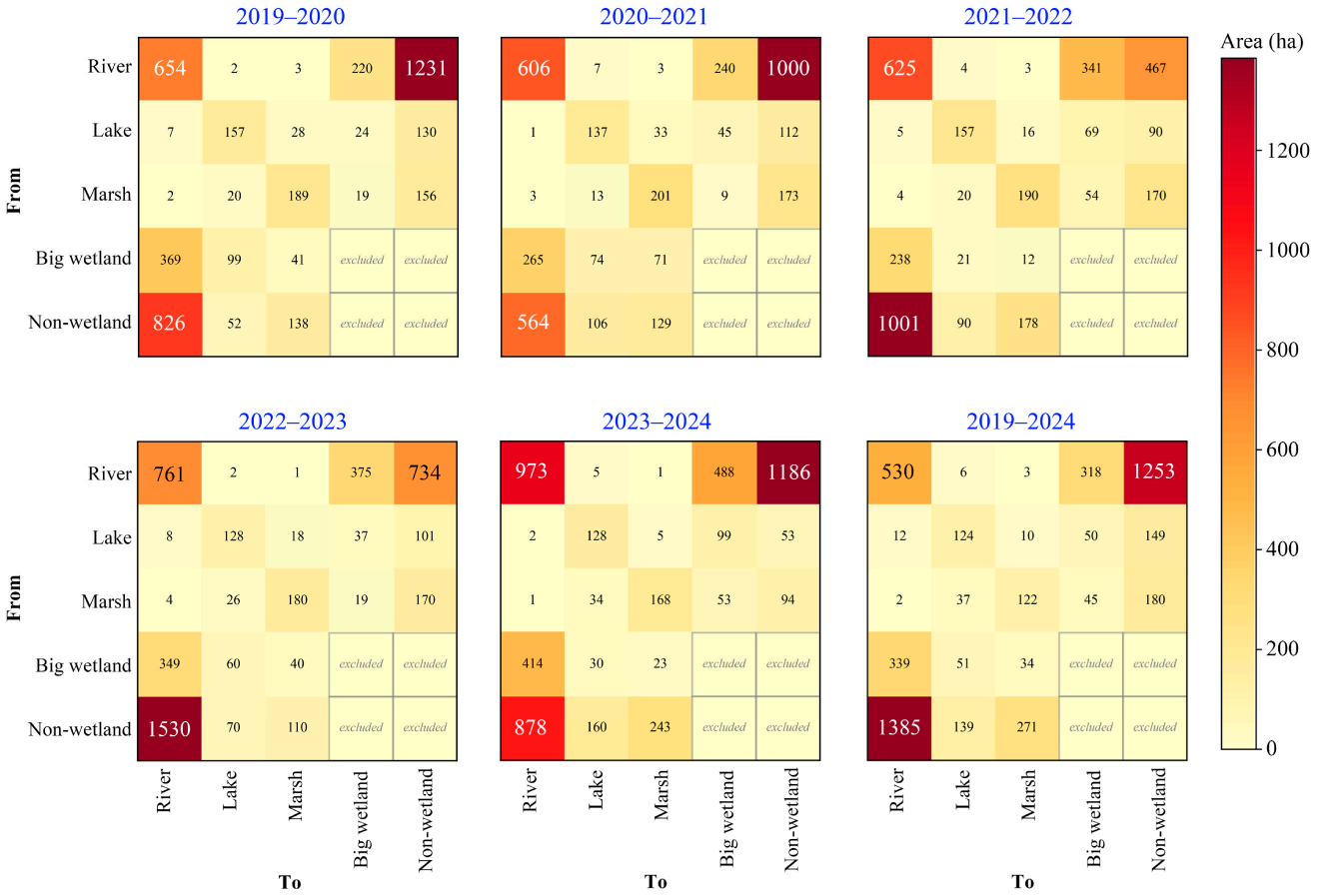


Figure 7. Transition matrix of SMWs in the ULB.

3.5. Conversion Characteristics of SMWs

The 2019–2024 transition matrix (Figure 7) showed that conversion to non-wetland was the main loss pathway for both river and marsh wetlands. Cumulative conversion to non-wetland reached 1252.85 ha for river wetlands and 179.60 ha for marsh wetlands. River wetlands also gained 338.62 ha from larger wetlands, indicating fragmentation of larger wetland bodies into SMW patches. The conversion of river wetlands to non-wetland peaked at 1231.15 ha in 2019–2020, decreased to 467.06 ha in 2021–2022, and rose again to 1186.02 ha in 2023–2024, indicating renewed degradation pressure in the final interval. Conversion from lake wetlands to marsh wetlands reached 33.30 ha in 2020–2021, higher than in the other intervals and consistent with a pronounced paludification process. Although 1384.78 ha of non-wetland converted to river wetlands over 2019–2024, this gain represented only 87.69% of the total river-wetland loss (1579.21 ha, including conversion to non-wetland, large wetland, lake, and marsh), indicating that recovery did not fully offset degradation.

Annual area and patch number were calculated from the extracted SMWs dataset. A 1 km × 1 km regular grid was then overlaid on the study area, and changes in wetland area within each grid cell were calculated to characterize the spatial distribution of trends. Table 3 summarizes the grid-level change classes. Stable grids dominated, accounting for 94.94% of all grid cells and 483,898.75 ha. Slight-increase and significant-increase grids accounted for 3.12% (15,880.27 ha) and 0.37% (1897.64 ha), respectively, whereas slight-decrease and significant-decrease grids accounted for 1.43% (7290.94 ha) and 0.14% (699.13 ha), respectively. Overall, increasing grids represented 3.49% of the study area (17,777.91 ha), compared with 1.57% (7990.07 ha) for decreasing grids.

Spatial distribution patterns of changing trends for SMWs in the ULB are illustrated in Figure 8.

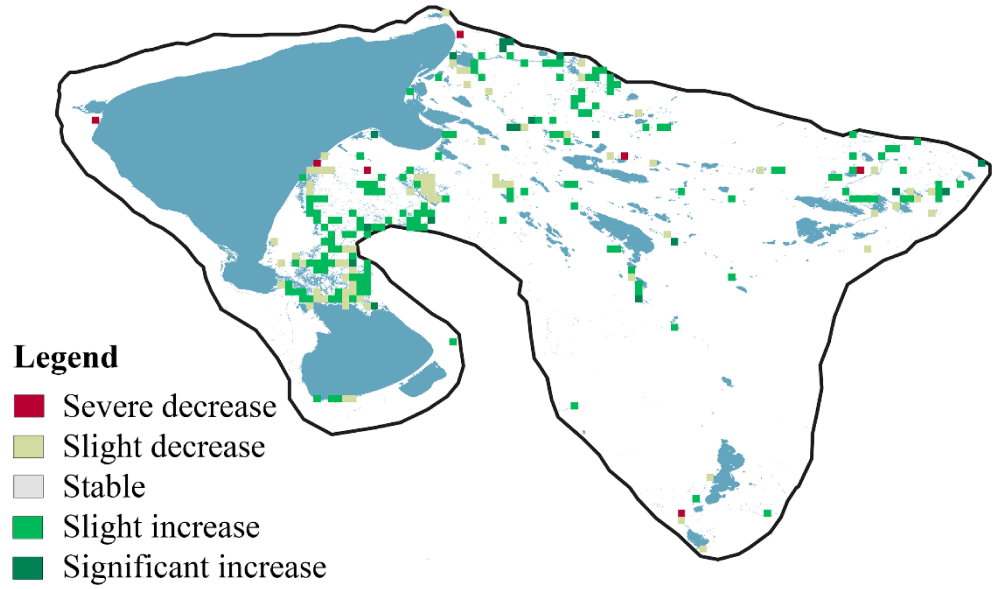


Figure 8. Spatial distribution of changing trends for SMWs.

As shown in Figure 8, areas classified as significant increase or slight increase were concentrated mainly along the shores of the Ulungur Lake and the Jili Lake, in low-lying depressions between the lakes, along rivers and ditches, and in seasonally moist zones. Increasing areas were particularly dense along the northern, northeastern, eastern, and southeastern shores of the Ulungur Lake, with additional high patch densities around the Jili Lake and in the low-lying transition zone between the two lakes. In contrast, areas classified as slight decrease generally occurred adjacent to increasing zones and formed connected patches of limited spatial extent. Areas classified as significant decrease showed no obvious clustering pattern.

3.6. Factors Influencing the Variation of SMWs

Figure 9 illustrates the factor detector results of SMWs in the ULB. Comparison of the 1, 5, and 10 km grid scales showed that the 10 km grid had the highest absolute q-values, but the ranking of factors differed among scales: at 10 km, DEM had the greatest independent explanatory power ($0.198 < q < 0.256$) and was significant in every year, whereas at 1 and 5 km ET, prec, temp, and CLCD were significant and had higher q-values than DEM. DEM dominance is therefore scale-dependent and holds at the 10 km regional scale; at the 1–5 km local scales, climate and land cover are more important. At 10 km, slope had q-values of 0.11–0.21 and was significant from 2019 to 2022 but not in 2023–2024; ET, CLCD, prec, temp, aspect, and light were not independently significant. Temporally, DEM reached its highest q-value (0.26) in 2019 and remained between 0.20 and 0.23; slope peaked at 0.21 in 2020 and declined to 0.11 in 2024; ET increased from 0.16 in 2019 to 0.17 in 2024; prec peaked at 0.16 in 2023 and declined to 0.06 in 2024; temp peaked at 0.19 in 2021 and then decreased; CLCD remained between 0.07 and 0.09.

The interaction detector was further used to evaluate the joint effects of paired factors (Figure 10). Of the 168 factor pairs, 114 showed nonlinear enhancement, 12 bivariate enhancement, and 42 univariate weakening; most pairs therefore showed enhancement, but this should not be interpreted directly as evidence of multifactor control. DEM–ET had q-values of 0.62, 0.56, and 0.70 in 2020, 2021, and 2023; it was the strongest pair in 2020 but not in 2021 (prec–DEM, 0.588) or 2023 (ET–slope, 0.747). ET–slope was especially strong in 2022 and 2024 (0.64 and 0.60). DEM–aspect remained high and stable, ranging from 0.489 to 0.585. ET–temp reached 0.63 in 2023 and 0.54 in 2024. Prec–DEM and prec–

slope reached 0.59 and 0.57 in 2021. Among interactions involving CLCD, CLCD–DEM had the highest explanatory power (0.41–0.50), followed by CLCD–slope and CLCD–ET. Interactions involving light showed nonlinear enhancement, but the single-factor *q*-value of Light was zero, and the interaction *q*-value equaled that of the paired factor, indicating no actual synergistic contribution.

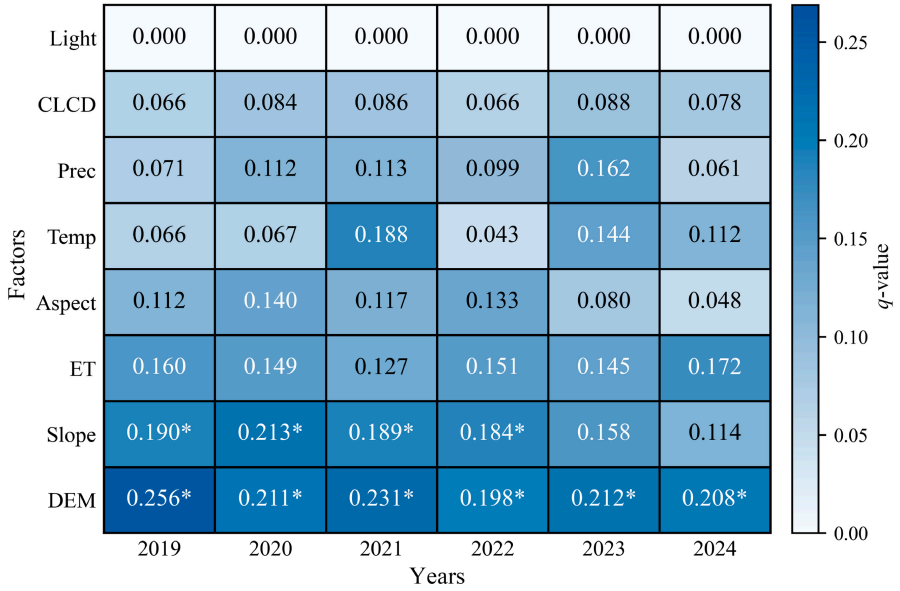


Figure 9. Factor detector results of SMWs in the ULB. *: $p < 0.05$ (significance).

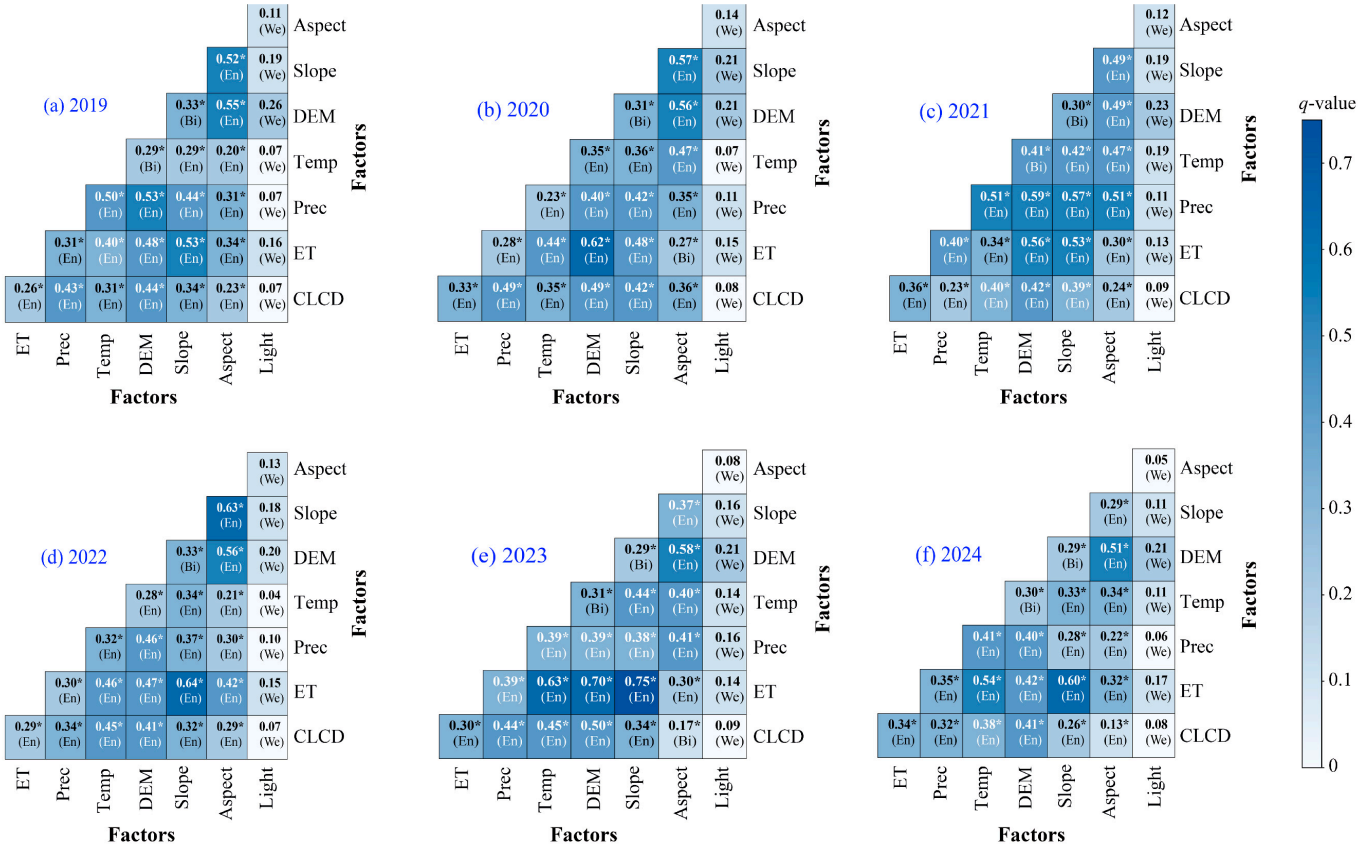


Figure 10. The q-value of interactions between driving factors: (**a**) 2019; (**b**) 2020; (**c**) 2021; (**d**) 2022; (**e**) 2023; (**f**) 2024. *: significant; En: Nonlinear enhancement; Bi: Bivariate enhancement; We: Univariate weakening; In: Independent.

Interaction *q*-values varied among years, but DEM–ET, DEM–aspect, and ET–slope remained above 0.40 throughout the study period, indicating relatively strong temporal stability. Overall interaction strength was highest in 2023, when seven factor pairs had *q*-values above 0.50. The years 2020 and 2021 each contained four such pairs, whereas only one or two pairs exceeded 0.50 in 2019, 2022, and 2024.

4. Discussion

4.1. Feature Selection Using Boruta and ACO

The present work revealed that Boruta identified all 19 candidate features as significant in the pooled multi-year dataset, whereas the accuracy-oriented ACO algorithm retained only DEM, NDWI, B12, TCW, and B8_contrast, reducing the feature set by 73.7%. These five variables were selected by both algorithms and jointly represented topographic, water/moisture, and textural information. In related wetland remote-sensing studies, Liu et al. [40] retained 18 of 32 features using RF, a study of Honghu Lake wetland in Hubei [41] retained 13 features after RF-based optimization, and Zhao et al. [42] selected eight features with Boruta compared with 16 using recursive feature elimination. The present results therefore show relatively strong feature-compression efficiency. Boruta is designed to retain all statistically relevant information [43,44], whereas the global-search capability of ACO promotes a more parsimonious subset [45,46].

Compared with methods based only on individual feature rankings or linear dimensionality reduction [47], combining statistical relevance screening with intelligent optimization provides a balance between reliability and discriminative contribution. Because Boruta retained all 19 features in the pooled dataset, the Boruta–ACO overlap is simply the ACO subset (DEM, NDWI, B12, TCW, and B8_contrast), not independent convergence of two methods. The comparison remains informative as a contrast between all-relevant screening and parsimonious selection: five ACO features achieved accuracy comparable to the 19-feature set (OA 0.923 vs. 0.926). At the annual scale, the ACO subsets varied in size and composition, indicating temporal instability in year-specific feature selection [48].

4.2. Comparison of Temporal Robustness Among Multi-Strategy Machine Learning Models

Wetland remote sensing studies commonly pair a single classifier with a single feature selection method, and systematic comparisons of classifier-feature combinations and cross-year generalization remain limited. In the present study, Boruta and ACO were combined with RF, XGBoost, and SVM algorithms under year-by-year independent and multi-year integrated modeling frameworks. Under year-by-year modeling, ACO reduced the feature count by 40–74%, while mean OA decreased by only 0.004 for RF and 0.009 for XGBoost, and the SD of both classifiers declined. These results indicate that compact ACO subsets retained most discriminative information while improving interannual stability.

Comparable studies reported an OA of 0.86 for XGBoost in Sentinel-2-based coastal wetland classification [49], F1 scores of 0.72 and 0.73 for RF and XGBoost in national-scale wetland mapping in New Zealand [50], an OA of 0.91 for RF in iSimangaliso Wetland Park [51], an OA of 0.88 for RF in multi-temporal Sentinel-2 classification of aquatic vegetation in temperate wetlands, an OA of 0.90 for XGBoost in mapping herbaceous plant communities in Poyang Lake wetlands [52], and an OA of 0.92 for XGBoost in coastal wetland mapping in the Pearl River Estuary [53]. Across the tested configurations, OA ranged from 0.87 to 0.93. Under the integrated strategy, Boruta+XGBoost and ACO+XGBoost achieved the highest mean OA, whereas SVM had the lowest mean OA. ACO+XGBoost provided a mean OA of 0.923 and an SD of 0.006; the paired comparison with ACO+RF showed a small, non-significant difference (Supplementary Table S7). Because accuracy

comparisons across regions, sensors, and class schemes are not strict benchmarks, we do not use them to rank the present model against other studies.

4.3. Distinctiveness of the Driving Mechanisms of SMWs Change

The GD is widely used to investigate wetland driving factors, but many applications are conducted at a single spatial scale and give limited consideration to scale effects [54,55]. To evaluate scale dependence in the ULB, this study used 1 km, 5 km, and 10 km grids representing the local micro-environment, landscape unit, and regional background, while also considering the native resolutions of the driving datasets. The 10 km scale had the highest absolute q-values, but the ranking of factors differed among scales. At 10 km, DEM had q-values of 0.20–0.26, was the strongest factor in every year, and remained significant throughout the study period, exceeding values reported for the Yellow River Source Region (0.205) [56] and national wetland parks in the Yellow River Basin [55]. At 1 and 5 km, however, ET, Prec, Temp, and CLCD were significant and had higher q-values than DEM; DEM was significant in 5 of 6 years at 1 km and 3 of 6 years at 5 km. DEM dominance therefore holds at the regional (10 km) scale, whereas climate and land cover are more important at the local (1–5 km) scale. At 10 km, 46.8% of the 2024 SMW area lay in the 480–500 m band and 95% below 600 m; the mean slope of SMW pixels was 1.82°, with 66.0% on slopes $< 2°$ and 98.4% on slopes $< 5°$. ET increased with elevation from about 100 at 450–480 m to 128 at 550–600 m; DEM controls where water converges and ET controls the loss term, and their joint q reached 0.696 in 2023. Slope had q-values of 0.11–0.21 in the early years, broadly consistent with previous studies [57,58], whereas ET was not independently significant in any year [59], illustrating regional differences in dominant wetland controls. Pairwise interaction detection showed enhancement for all factor combinations. DEM–ET reached a maximum q-value of 0.70, while DEM–Aspect remained between 0.489 and 0.558. These values are comparable to interaction strengths reported in the Poyang Lake Basin [60] and the Yellow River Delta [57]. Because pairwise q-values exceeded the larger individual q-value and most combinations showed nonlinear enhancement, the results support multifactor control of SMWs spatial differentiation. Interactions involving light did not provide additional explanatory power because its single-factor q-value was zero, suggesting a limited independent contribution from this human-activity proxy in the study area. This differs from the Three Gorges Reservoir area, where human activities reportedly explained more than 10% of wetland variation [61].

Overall, unlike wetlands in humid regions, where climatic and anthropogenic controls are often dominant, SMWs in the ULB appear to be most strongly constrained by micro-topography. The Geographical Detector analysis identified DEM as a primary driver of SMW changes. The independent explanatory power of DEM was higher than that reported for wetlands in the Yellow River Source Region and the Yangtze River Basin, reflecting the sensitivity of shallow SMWs in arid regions to elevation and drainage patterns. However, topography shapes the evolution of SMWs primarily by redistributing surface and subsurface water in this arid basin. Elevation and slope govern runoff convergence: depressions and gentle lowlands capture overland flow and host groundwater seepage, whereas steep sites drain rapidly and rarely sustain standing water. Microtopography further controls groundwater depth; low-lying zones maintain shallow groundwater to sustain wet conditions, while higher positions experience deep groundwater and wetland desiccation. As such, topography provides the fundamental physical framework for water redistribution, governing the distribution, persistence and interannual dynamics of SMWs.

Human-activity factors did not show significant independent explanatory power, differing from findings for SMWs in eastern plains and peri-urban areas of China. Nevertheless, human activities may still interact with topography and climate by altering evapotranspi-

ration and surface runoff and thereby indirectly contribute to wetland degradation. The enhancement observed for all factor interactions indicates that spatial differentiation of SMWs results from the combined effects of topographic conditions, hydrothermal processes, and human disturbances rather than from any single factor alone.

5. Conclusions

This study established an integrated analytical framework combining feature optimization, model comparison, spatiotemporal dynamics analysis, and investigation of driving mechanisms for SMWs in the ULB in Xinjiang. The main conclusions are as follows:

1. ACO identified five cross-year stable features: DEM, NDWI, B12, TCW, and B8_contrast. These variables represent the principal discriminative dimensions of topography, water and moisture conditions, and texture.
2. The multi-year integrated modeling framework provided a slightly higher mean accuracy and a slightly lower SD than year-by-year modeling. The ACO+XGBoost scheme provided the best overall balance of accuracy and stability, with a six-year mean OA, Kappa, and Macro F1-score of 0.923, 0.903, and 0.919, respectively, demonstrating high cross-year robustness and generalization capacity.
3. From 2019 to 2024, the total area of SMWs in the ULB showed a fluctuating overall increase. These wetlands were concentrated mainly in lakeshore zones, along river channels and ditches, and in low-lying water-collecting landforms. Degradation and recovery of SMWs occurred simultaneously, but the cumulative magnitude of degradation exceeded that of recovery. Sustained expansion occurred in only a limited number of patches along lakeshores and watercourses, while 94.94% of the basin remained stable in terms of the wetland spatial pattern.
4. Results of the factor detector indicated that, at the 10 km analytical scale, DEM was the dominant factor explaining the spatial differentiation of SMWs, whereas climate and land cover were more important at 1–5 km scales. Results of the interaction detector indicated that most pairwise interactions showed enhancement, with DEM–ET producing the strongest joint explanatory power in 2020; 42 pairs showed univariate weakening. These results indicate that the spatial pattern of SMWs in this arid basin is governed mainly by interactions between topographic conditions and regional hydrothermal processes. Direct human and hydrological drivers were not included, so the role of human activity cannot be determined from the present data.

Supplementary Materials: The following supporting information can be downloaded at: https://www.mdpi.com/article/10.3390/w18212718/s1, Table S1: Annual sample totals and training/validation split; Table S2: Sample counts by year and class; Table S3: OPGD discretization scheme; Table S4: SVM accuracy with fixed C = 1 and after tuning; Table S5: Per-class precision, recall, F1, and support; Table S6: Leave-one-year-out cross-validation accuracy; Table S7: Paired comparison of pooled ACO+XGBoost and ACO+RF; Table S8: SMW area under different lower size thresholds; Table S9: Factor detector results at 1, 5, and 10 km.

Author Contributions: Conceptualization, M.E. and S.A.; methodology, M.E. and S.A.; software, S.A.; validation, M.E., S.A. and L.G.; formal analysis, S.A.; investigation, S.A. and L.G.; resources, M.E. and S.A.; data curation, M.E.; writing—original draft preparation, S.A. and M.E.; writing—review and editing, S.A. and M.E.; visualization, S.A.; supervision, M.E.; project administration, M.E.; funding acquisition, M.E. All authors have read and agreed to the published version of the manuscript.

Funding: This research was funded by the Tianshan Talent Training Program, under Grant 2024TSYCJU0004, and the Natural Science Foundation of Xinjiang Uygur Autonomous Region under Grant 2023D01E08.

Data Availability Statement: The data that support the findings of this study are available from the corresponding author on request.

Conflicts of Interest: The authors declare no conflicts of interest.

Abbreviations

The following abbreviations are used in this manuscript:

SMWs	Small and Micro Wetlands
ACO	Ant Colony Optimization
RF	Random Forest
XGBoost	Extreme Gradient Boosting
SVM	Support Vector Machine
GD	Geographical Detector
ULB	Ulungur Lake Basin
GEE	Google Earth Engine
NDVI	Normalized Difference Vegetation Index
EVI	Enhanced Vegetation Index
NDWI	Normalized Difference Water Index
MNDWI	Modified Normalized Difference Water Index
NDMI	Normalized Difference Moisture Index
GLCM	Gray Level Co-Occurrence Matrix
ASM	Angular Second Moment
DEM	Digital Elevation Model
Temp	Annual Mean Temperature
Prec	Annual Precipitation
ET	Evapotranspiration
CLCD	China Land Cover Dataset
OA	Overall Accuracy

References

1. Szpakowska, B.; Świerk, D.; Dudzińska, A.; Pajchrowska, M.; Gołdyn, R. The influence of land use in the catchment area of small waterbodies on the quality of water and plant species composition. *Sci. Rep.* **2022**, *12*, 7265. [CrossRef] [PubMed]
2. Wang, L.L.; Mamattursun, E.; Hu, Y.L.; Xayida, S. Health risk assessment of heavy metal(loid)s in the overlying water of small wetlands based on Monte Carlo simulation. *Toxics* **2024**, *12*, 488. [CrossRef] [PubMed]
3. Seekell, D.A.; Pace, M.L.; Tranvik, L.J.; Verpoorter, C. A fractal-based approach to lake size-distributions. *Geophys. Res. Lett.* **2013**, *40*, 517–521. [CrossRef]
4. Holgerson, M.A.; Raymond, P.A. Large contribution to inland water CO_2 and CH_4 emissions from very small ponds. *Nat. Geosci.* **2016**, *9*, 222–226. [CrossRef]
5. Hunter, M.L.; Acuña, V.; Bauer, D.M.; Bell, K.P.; Calhoun, A.J.; Felipe-Lucia, M.R.; Fitzsimons, J.A.; González, E.; Kinnison, M.; Lindenmayer, D. Conserving small natural features with large ecological roles: A synthetic overview. *Biol. Conserv.* **2017**, *211*, 88–95. [CrossRef]
6. Chen, M.L.; Maimaitituerxun, A.; Wang, L.L.; Hu, Y.L. Pollution and potential risk assessment of heavy metals in small wetlands in the Bosten Lake Basin. *Arid Land Geogr.* **2025**, *48*, 211–2121.
7. Wang, N.; Zhang, K.; Luo, J.; Mohamed, O.; Duan, H.; Dash, J. Use of multi-source remote sensing data to understand long-term wetland dynamics and water environment responses in the Chaohu Lake Basin. *Remote Sens.* **2026**, *18*, 2646. [CrossRef]
8. Huang, Y.Q.; Zhang, X.Y.; Yu, H.; Shen, M.Y.; Li, S.Y.; Li, R.; Zhang, J.; Zhang, X.D.; Yan, S.; Zhang, W.G. Landscape pattern changes and driving mechanisms of small wetlands in western Jilin. *Chin. J. Ecol.* **2026**, *45*, 434–447.
9. Roy, D.P.; Wulder, M.A.; Loveland, T.R.; Woodcock, C.E.; Allen, R.G.; Anderson, M.C.; Helder, D.; Irons, J.R.; Johnson, D.M.; Kennedy, R. Landsat-8: Science and product vision for terrestrial global change research. *Remote Sens. Environ.* **2014**, *145*, 154–172. [CrossRef]
10. Martina, N.; Sara, M.; Domenico, D.; Gabriëlle, D.L.; Susan, S.D.; Alessia, F.; Alessio, D.; Christian, M. Field-scale irrigation estimation using Sentinel-1 and Sentinel-2 data within a soil water balance model coupled to the Water Cloud Model. *Remote Sens. Environ.* **2026**, *346*, 115639. [CrossRef]
11. Wei, X.; Xu, W.; Wang, L.; Guo, R.; Duan, Z. An interpretable Earth observation framework for estimating lake dissolved organic carbon in Sweden using Sentinel-2 and ERA5-Land data. *Int. J. Appl. Earth Obs. Geoinf.* **2026**, *152*, 105488. [CrossRef]

12. Li, C.; Cui, H.; Tian, X. Remote sensing image segmentation of wetlands in Macau based on machine learning. *J. Phys. Conf. Ser.* **2023**, *2665*, 012006. [CrossRef]
13. Gao, Y.K.; Zhao, D.; Liang, B.; Yang, X.Y.; Xue, X. Remote sensing monitoring of soil salinization based on Bootstrap-Boruta feature stability assessment: A case study in Minqin Lake Region. *Remote Sens.* **2026**, *18*, 245. [CrossRef]
14. Lai, Q.; Wu, D. Automated landscape zoning planning for national parks by integrating the Invest model and ant colony optimization algorithm: A case study of Nanling National Park. *Front. For. Glob. Change* **2026**, *9*, 1826156. [CrossRef]
15. Pal, M. Random Forest classifier for remote sensing classification. *Int. J. Remote Sens.* **2005**, *26*, 217–222. [CrossRef]
16. Zhai, G.Q.; Du, J.Q.; Li, L.J.; Zhu, X.Q.; Song, Z.B.; Wu, L.Y.; Chong, F.F.; Chen, X.Y. Spatiotemporal dynamics and driving factors of small and micro wetlands in the Yellow River basin from 1990 to 2020. *Remote Sens.* **2024**, *16*, 567. [CrossRef]
17. Deng, Q.; Shao, X.; Zhang, X.; Fan, Z.; Zhao, Y.; Zhou, L.; Hu, Z.; Dou, L.; Li, S. Spatiotemporal monitoring of small and micro wetlands for urban ecological security assessment: A case study of Linyi City, China. *Ecol. Indic.* **2026**, *189*, 115210. [CrossRef]
18. Guo, H.Y.; Cao, C.X.; Xu, M.; Yang, X.W.; Chen, Y.Y.; Wang, K.M.; Robert, S.D.; Li, J.B.; Gao, X.T. Spatiotemporal distribution pattern and driving factors analysis of GPP in Beijing-Tianjin-Hebei region by long-term MODIS data. *Remote Sens.* **2023**, *15*, 622. [CrossRef]
19. Zou, K.B.; Zhang, Y.H.; Liu, X.W.; Xue, S.H.; Yang, B.W.; Cui, Y.X. Response of agricultural nonpoint source pollution load in the Ulungur River basin under climate change. *Arid Zone Res.* **2022**, *39*, 625–637.
20. Song, Y.; Huo, Q.; Zi, F.; Ge, J.; Qiu, X.; Yun, L.; Gulden, S.; Yang, L.; Wang, B.; Chen, S. Macrobenthic community structure and water quality evaluation in Ulungu River Basin (Northwest China). *Water* **2024**, *16*, 918. [CrossRef]
21. Liu, Y.Z.; Li, Y.Z.; Zhu, Y.J.; Tang, Z.W.; Yu, J.B.; Wang, X.H.; Guan, B.; Zhou, D.; Wang, S.W. Spatiotemporal effects of atmospheric correction on fractional vegetation coverage retrieval in coastal wetlands based on the pixel dichotomy model. *Wetl. Sci.* **2026**, *24*, 249–261.
22. Usman, M.; Chua, L.H.C.; Irvine, K.N.; Teang, L. Estimating water surface elevation for a wetland using integrated multi-sourced remote sensing data. *Wetl. Ecol. Manag.* **2025**, *33*, 20. [CrossRef]
23. Li, T.; Wu, Y.; Ren, F.; Li, M.Y. Estimation of unrealized forest carbon potential in China using time-varying Boruta-SHAP-random forest model and climate vegetation productivity index. *J. Environ. Manag.* **2025**, *377*, 124649. [CrossRef] [PubMed]
24. Al-Ruzouq, R.; Shanableh, A.; Barakat, A.; Gibril, M.; AL-Mansoori, S. Image segmentation parameter selection and ant colony optimization for date palm tree detection and mapping from very-high-spatial-resolution aerial imagery. *Remote Sens.* **2018**, *10*, 1413. [CrossRef]
25. Belgiu, M.; Drăgut, L. Random Forest in remote sensing: A review of applications and future directions. *ISPRS J. Photogramm. Remote Sens.* **2016**, *114*, 24–31. [CrossRef]
26. Ma, X.; Ding, C.; Luan, S.; Wang, Y.; Wang, Y. Prioritizing influential factors for freeway incident clearance time prediction using the gradient boosting decision trees method. *IEEE Trans. Intell. Transp. Syst.* **2017**, *18*, 2303–2310. [CrossRef]
27. Zuo, R.; Carranza, E.J.M. Support Vector Machine: A tool for mapping mineral prospectivity. *Comput. Geosci.* **2011**, *37*, 1967–1975. [CrossRef]
28. Piaser, E.; Villa, P. Evaluating capabilities of machine learning algorithms for aquatic vegetation classification in temperate wetlands using multi-temporal Sentinel-2 data. *Int. J. Appl. Earth Obs. Geoinform.* **2023**, *117*, 103202. [CrossRef]
29. Huang, W.C.; Fei, X.Y.; Yang, W.W.; Wang, Z.; Gao, Y.J.; Yan, H. A study on the classification of coastal wetland vegetation based on the Suaeda salsa index and its phenological characteristics. *Ecol. Indic.* **2025**, *170*, 113021. [CrossRef]
30. Ren, D.; Qiu, X.; An, Z. A multi-source data-driven analysis of building functional classification and its relationship with population distribution. *Remote Sens.* **2024**, *16*, 4492. [CrossRef]
31. *GB/T 24708-2009*; Wetland Classification. General Administration of Quality Supervision, Inspection and Quarantine of the People's Republic of China. Standardization Administration of China: Beijing, China, 2009.
32. Sen, P.K. Estimates of the regression coefficient based on Kendall's tau. *J. Am. Stat. Assoc.* **1968**, *63*, 1379–1389. [CrossRef]
33. Mann, H. Nonparametric tests against trend. *Econom. J. Econom. Soc.* **1945**, *13*, 245–259. [CrossRef]
34. Zhang, J.Q.; Liu, Z.; Zhang, J.X.; Li, Q.; Tuo, B.F.; Bai, Y.; Lyu, J.J. Drought propagation mechanisms and spatial heterogeneity in the Yellow River Basin based on convergent cross mapping and the geographical detector method. *J. Hydrol. Reg. Stud.* **2026**, *67*, 103803. [CrossRef]
35. Wang, Y.L.; Zhang, W.J. Mechanisms driving surface wind speed increases in an ecologically fragile region of Northwest China: Insights from circulation anomalies and geographical detector analysis. *J. Arid Land* **2026**, *18*, 928–948. [CrossRef]
36. Song, Y.; Wang, J.; Ge, Y.; Xu, C. An optimal parameters-based geographical detector model enhances geographic characteristics of explanatory variables for spatial heterogeneity analysis: Cases with different types of spatial data. *GISci. Remote Sens.* **2020**, *57*, 593. [CrossRef]
37. *GB/T 42481-2023*; Specifications for Conservation and Management of Small Wetlands. Standardization Administration of China: Beijing, China, 2023.
38. Jensen, J.R. *Introductory Digital Image Processing: A Remote Sensing Perspective*, 4th ed.; Pearson: Upper Saddle River, NJ, USA, 2015.

39. Lehner, B.; Döll, P. Development and validation of a global database of lakes, reservoirs and wetlands. *J. Hydrol.* **2004**, *296*, 1–22. [CrossRef]
40. Liu, Z.; Hou, J.; Ji, W.; Huang, L.; Xing, L.; Zhu, H.; Han, Z. Wetland classification method in Dongying City based on combination optimization and random forest algorithm. *J. Univ. Jinan (Sci. Technol.)* **2025**, *39*, 819–827.
41. Xia, Y.; Li, E.; Wang, X.; Zhang, Y.; Yang, J.; Zhou, R. Application of Random Forest algorithm based on feature optimization in wetland information extraction: A case study of Honghu Wetland Nature Reserve in Hubei Province. *J. Cent. China Norm. Univ. (Nat. Sci.)* **2021**, *55*, 639–648.
42. Zhao, Y.B.; Peng, D.L.; Guo, F.M.; Wang, Y.; Huang, J.X. Estimating forest stock volume based on feature selection and machine learning. *J. Beijing For. Univ.* **2025**, *47*, 155–167.
43. Kursa, M.B.; Rudnicki, W.R. Feature selection with Boruta package. *J. Stat. Softw.* **2010**, *36*, 1–13. [CrossRef]
44. Al-Falluji, R.A.; Albahar, M.A. OEF-LULC: An optimized and explainable AI-based framework for land use land cover classification. *IEEE Access* **2026**, *14*, 38745. [CrossRef]
45. Sun, K.; Yin, S.L.; Liu, J. An improved ant colony algorithm used in Hyperspectral remote sensing image classification. *J. Shenyang Norm. Univ. (Nat. Sci.)* **2016**, *34*, 354.
46. Sun, Q.; Wu, Q.Y. Feature space fusion classification of remote sensing image based on ant colony optimisation algorithm. *Int. J. Inform. Commun. Technol.* **2022**, *20*, 164. [CrossRef]
47. Jolliffe, I.T.; Cadima, J. Principal component analysis: A review and recent developments. *Philos. Trans. Ser. A Math. Phys. Eng. Sci.* **2016**, *374*, 20150202. [CrossRef]
48. Ma, Y.; Ma, Y.; Zheng, Q.; Chen, Q. Dynamic co-optimization of features and hyperparameters in object-oriented ensemble methods for wetland mapping using sentinel-1/2 data. *Water* **2025**, *17*, 2877. [CrossRef]
49. Arij, N.; Latifi, H. Optimized wetland classification in arid coastal environments: Integrating sentinel-2 imagery with hyperparameter-tuned machine learning algorithms. *Int. Arch. Photogramm. Remote Sens. Spat. Inf. Sci.* **2026**, *XLVIII-4/W22-2025*, 7–14. [CrossRef]
50. Khan, M.S.I.; Vega-Corredor, M.C.; Wilson, M.D. Mapping wetlands with high-resolution planet SuperDove satellite imagery: An assessment of machine learning models across the diverse waterscapes of New Zealand. *Remote Sens.* **2025**, *17*, 2626. [CrossRef]
51. Chifurira, C.; Sieben, E.; Shandu, I.; Xulu, S. Comparative machine learning classification of a heterogeneous Ramsar wetland using sentinel-1 and sentinel-2 imagery with quantity and allocation disagreement diagnostics. *Front. Remote Sens.* **2026**, *7*, 1814582. [CrossRef]
52. Zhang, L.; Luo, W.; Zhang, H.; Duan, X.; Li, B. Classification scheme for mapping wetland herbaceous plant communities using time series sentinel-1 and sentinel-2 data. *Natl. Remote Sens. Bull.* **2023**, *27*, 1362–1375. [CrossRef]
53. Liu, Y.; Liu, K.; Cao, J. Classification of coastal wetlands in the pearl river estuary using zhuhai-1 hyperspectral imagery and XGBoost algorithm. *Bull. Surv. Mapp.* **2023**, *12*, 136–141.
54. Peng, N.; Zhou, L.Z. Analysis of wetland landscape pattern variation and its driving factors of Caizi Lake group based on GeoDetector. *Water Resour. Prot.* **2021**, *37*, 168–176.
55. Zhou, C.; Zhao, Y.L.; Ren, M.M. Spatiotemporal differentiation, center of gravity evolution and driving factors of national wetland parks in the Yellow River Basin. *Arid Land Geogr.* **2024**, *47*, 506–514.
56. Jiang, R.; Liu, J.; Liu, W.; Zhang, D.; Hu, W. Changes and driving forces analysis of alpine wetlands in the first meander of the Yellow River based on long-term time series remote sensing data. *Front. Ecol. Evol.* **2023**, *11*, 1193059. [CrossRef]
57. Yin, X.L.; Tan, C.Y.; Ke, Y.H.; Zhou, D.M. Evolution and driving factors of salt marsh wetland landscape pattern in the Yellow River Delta in 1973–2020. *Acta Ecol. Sin.* **2024**, *44*, 67–80.
58. Wei, C.; Guo, B.; Fan, Y.; Zang, W.; Ji, J. The change pattern and its dominant driving factors of wetlands in the Yellow River delta based on sentinel-2 images. *Remote Sens.* **2022**, *14*, 4388. [CrossRef]
59. Liu, J.P.; Gao, J.; Dong, C.Y. Regional differentiation and factors influencing changes in swamps in the Sanjiang Plain from 1954 to 2015. *Acta Ecol. Sin.* **2019**, *39*, 4821–4831. [CrossRef]
60. Zou, Y.Y.; Dong, X.B.; Liu, Y.F.; Wang, Y.L.; Gao, Y.; Fan, J.; Ding, B.B.; Zhuang, D.C.; Zhang, W. Analysis of the changes in water conservation in Jiangxi province from 2000 to 2020. *J. Res. Ecol.* **2023**, *14*, 940–950. [CrossRef]
61. Zhang, H.S.; Li, S.; Wang, Y.D.; Wang, Y.Q.; Zhang, J.; Li, J.J.; Cheng, S.B. Human activities intensify wetland landscape fragmentation in Three Gorges Reservoir area. *J. Soil Water Conserv.* **2025**, *39*, 139–151.

Disclaimer/Publisher's Note: The statements, opinions and data contained in all publications are solely those of the individual author(s) and contributor(s) and not of MDPI and/or the editor(s). MDPI and/or the editor(s) disclaim responsibility for any injury to people or property resulting from any ideas, methods, instructions or products referred to in the content.